Nanoscale

Accepted Manuscript

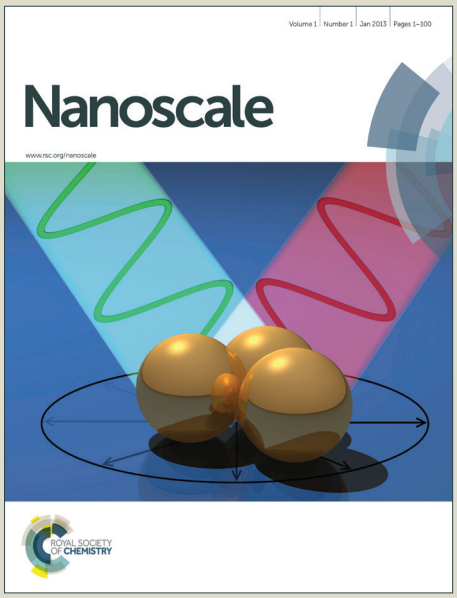

Cite this: DOI: 10.1039/c0xx00000x

www.rsc.org/xxxxxx

COMMUNICATION

Orientation-tuning in self-assembled heterostructures induced by a buffer layer

Yuanmin Zhu[a], Pingping Liu[a], Rong Yu[b] , Ying-Hui Hsieh[c], Dan Ke[a], Ying-Hao Chu[c,d], and Qian Zhan[a]*

Received (in XXX, XXX) Xth XXXXXXXXX 20XX, Accepted Xth XXXXXXXXX 20XX
DOI: 10.1039/b000000x

Anisotropic nano-plate structures in self-assembled perovskite-spinel $BiFeO_3$-$NiFe_2O_4$ and $BiFeO_3$-$CoFe_2O_4$ thin films which were deposited on $(001)_c$ $SrRuO_3/SrTiO_3$ and $DyScO_3$ substrates respectively have been demonstrated using transmission electron microscopy combined with strain analysis. Unlike the unitary cube-on-cube orientation relationship reported widely, the growth direction of the $CoFe_2O_4$ and $NiFe_2O_4$ plates were tuned to $[011]_c$ while the $BiFeO_3$ matrix kept $[001]_c$ in both systems. Especially, a thin stress-sensitive $BiFeO_3$ buffer layer between the spinel nanostructure and the substrate was introduced for providing a complex strain state in both film systems. The novel orientation tuning and the pattern configuration of the heterostructures are mainly attributed to the strain imposed on the films and the anisotropic ledge growth mechanism of spinels.

1. Introduction

Complex oxides cover a wide range of intriguing functionalities induced by the interplays among the lattice, charge, orbital and spin degrees of freedom and offer tremendous opportunities to develop next generation electronic devices.[1-3] Among complex oxide heterostructures, the vertical nanocomposite architecture has drawn a considerable spotlight and been used to tune the functionalities benefitting from their plentiful hetero-interfaces, e.g. $BiTiO_3$-$CoFe_2O_4$, $BiFeO_3$-$CoFe_2O_4$[4, 5], $PbTiO_3$-$CoFe_2O_4$[6], $BiTiO_3$-Sm_2O_3[7], $La_{0.7}Sr_{0.3}MnO_3$-CeO_2[8] etc. The unique physical properties of materials can be tuned through structure modification which is a fundamental topic often to be addressed.

Thermodynamics and kinetics affecting the evolutions of these nanostructures are various and complicated, such as elastic energy, crystal structure, interface energy, growth parameters and heat treatment.[9-13] For epitaxial thin films, elastic strain energy, commonly induced by the epitaxial constraints along the heterointerfaces due to lattice mismatch, is demonstrated to be a vital factor controlling the growth of heterostructures.[14, 15] The strain affects chemical bond length and angles, defect types and densities such as dislocation, oxygen vacancies, thus manipulating corresponding physics of the nanostructures.[16] Through theoretical and experimental investigations in the classic vertical nanostructures, Roytburd et al suggested a general way of controlling the phase architectures by elastic interactions between substrates and films.[17, 18] Previous studies mainly focused on the vertical heterostructures with a simple cube-on-cube orientation relationship between the constituent phases and the substrate, that is [001]//[001] and (100)//(100).[19-25] Recently, a significant attempt to control the relative orientations in the two-phase heterostructures by stain engineering using substrates with different crystal structures and lattice parameters was introduced.[26] Exploring wider manipulations for crystallographic orientations and hetero-interfaces in complex oxide vertical nanostructures becomes extremely important.

In the present paper, rather than the unitary cube-on-cube crystallographic orientations, periodic plate-configurations of two-phase nanostructures induced by a buffer layer were observed by transmission electron microscopy (TEM). Perovskite $BiFeO_3$ (BFO) and spinel $NiFe_2O_4$ or $CoFe_2O_4$ (NFO, CFO) self-assembled heteroepitaxial nanostructures were chosen as the model systems. The interfacial structures at an atomic scale and the underline growth mechanisms were discussed in detail. Two key points have to be emphasized to realize the controllable orientation tuning by strain engineering in the vertical heterostructure thin films. First of all, a buffer layer of BFO who has been demonstrated to be a high stress sensitivity in many pioneer works[27-29] was introduced intending to tune the orientation of nanostructures. Secondly, perovskite substrates with the lattice parameters close to BFO were selected in order to facilitate highly coherent heteroepitaxial strain in BFO.

2. Experimental

Perovskite-spinel $BiFeO_3$-$NiFe_2O_4$ and $BiFeO_3$-$CoFe_2O_4$ heteroepitaxial nanostructures were grown on single crystal $(001)_c$ $SrTiO_3$ and $(001)_c$ $DyScO_3$ substrates respectively by pulsed laser deposition at 700 ℃ under an oxygen pressure of 200 mTorr (subscript c represents cubic/pseudocubic structure). Both composite targets were used with a molar ratio of 0.65BFO:0.35NFO/CFO. BFO is a rhombohedrally distorted perovskite structure with the space group of *R3c* that can be described as a pesudocubic cell, a_c=3.962 Å[30]. NFO and CFO are magnetic spinels with cubic Fd3m structure (a_{NFO}=8.34 Å, a_{CFO}=8.38 Å)[31, 32]. BFO-CFO and BFO-NFO systems show similar structure characteristic[21], thus the results are discussed together in the present study. $SrTiO_3$ (STO) substrate for the growth of BFO-NFO film is a cubic perovskite structure, on which a 30 nm thick $SrRuO_3$ (SRO) epilayer was grown for

decreasing the lattice mismatch with BFO. The strain in the 30 nm thick SRO layer has been relaxed to a large extent estimated from the critical thickness. SRO has the lattice parameters of a_o=5.5943 Å, b_o=5.5708Å, c_o=7.8810Å (pesudocubic lattice a_c=3.9405 Å[33]) (subscript o represents orthorhombic structure). $DyScO_3$ (DSO) with lattice parameters of a_o=5.4494 Å, b_o=5.7263Å, c_o=7.9132Å (a_c=3.940 Å[34]) was chosen to be the substrate for another similar system of BFO-CFO nanocomposite film. DSO and SRO as the direct contact surfaces for the growth of films are orthorhombic (*Pbnm* 62) distorted perovskite structure, having the nominal misfit of ~0.55% with the BFO matrix. The following indexing and discussion on the perovskite structures were referred to the pseudo-cubic unit cell for simplicity.

Cross-section as well as plan-view samples for TEM were prepared by a standard procedure of TEM sample preparation. Macro- and microstructures of the films were investigated using an FEI TECNAI F20 with an information limit of 1.4 Å and a JEOL-2010 microscope operating at 200 kV. Chemical analysis was also carried out using the F20 microscope equipped with Energy Disperse X-Ray Detector (EDX).

3. Results and discussion

The low magnification morphologies and corresponding electron diffraction patterns (EDPs) of self-assembled BFO-NFO nanostructures grown on (001)-oriented SRO/STO substrates are given in Figure 1. Two dimensional (2-D) maze-like NFO nanostructures were embedded homogeneously in BFO matrix, as shown in Fig. 1a and 1c. Plate-shaped NFO elongated along $<011>_{NFO}$ direction with the average length (L) of ~450 nm and the width (W) about 35 nm, that the aspect ratio of L/W is around 13. They grew perpendicularly to the substrate and exhibited vertical interface with BFO matrix. $\{111\}_{NFO}$ facets formed out of the film surface for nanostructured NFO, confirmed by the following high resolution transmission electron microscopy (HRTEM) image. As seen from the plan-view EDP (Fig. 1b), two sets of mutually perpendicular [011]-oriented patterns of NFO phase were determined to be [011](0-22)NFO// [001](010)BFO //[001](010)STO and [011](0-22)NFO //[001](100)BFO// [001](100)STO, in accordance to the 2-D morphology revealed in Fig. 1a. The cross-sectional EDP in Fig. 1(d) demonstrates that BFO matrix kept $[001]_c$ growth direction matching the $[001]_c$ orientated perovskite substrate while NFO plate was tuned to $[011]_{NFO}$, obtaining the out-of plane orientation relationship of [0-11](022)NFO // [010](001)BFO // [010](001)STO. The vertical interface between BFO and NFO phases lies on {100}NFO/{100}BFO planes. It's clear that the pattern configuration and the crystallographic orientation of NFO nanostructure in this typical perovskite-spinel system are different from previous studies.

Figures 2a and 2c show the configuration of $BiFeO_3$-$CoFe_2O_4$ nanocomposite thin films from both plan-view and cross-section orientations. They were grown on $(001)_c$ single crystal DSO substrates that has an orthorhombic distorted perovskite structure. $CoFe_2O_4$, having the same spinel structure with NFO, was found to be included in $BiFeO_3$ matrix. Unlike above 2-D BFO-NFO system, however, CFO nanostructure elongated only along one direction of $[0\text{-}11]_{CFO}/[010]_{BFO}$ and exhibited a short and thick rectangular shape with aspect ratio (L/W) of 2.83. The growth direction of CFO was along $[011]_{CFO}$ while BFO matrix remained $[001]_c$ orientation, as the same as above BFO-NFO/SRO/STO system. $\{111\}_{CFO}$ facets and {100} vertical interfaces were also observed in the BFO-CFO/DSO thin films. The orientation relationships between BFO and CFO as well as DSO substrate can be determined to be [011](0-22)CFO // [001](010)BFO // $[001](010)_c$DSO for in plane [Fig. 2(b)] and [0-11](022)CFO // [010](001)BFO // $[010](001)_c$DSO for the out of plane direction [Fig. 2(d)].

On $(001)_c$ SRO/STO and DSO perovskite surfaces, $[011]_{CFO/NFO}$-orientated CFO/NFO nanostructures can be observed in both systems with BFO matrix keeping $[001]_c$ growth direction, demonstrating novel nanostructure configurations and crystal growth model. Note that NFO and CFO nanostructures preferred to elongate along its <110> direction. Such a growth behavior for the spinel structure can be ascribed to the ledge preferential growth induced by the anisotropic arrangement of cations along the <110> direction in spinel structure[35]. Meanwhile, distinct difference was observed in the two similar systems: one dimensional and 2-D plate distributions of nanostructures with different aspect ratios developed in BFO-CFO/DSO and BFO-NFO/SRO/STO systems, respectively. Intrinsic microstructural features should be investigated further to reveal such an unusual phenomenon.

To shed light on the intriguing growth of the nanostructures, HRTEM was carried out to show the interface structure at an atomic scale. The interface structure between NFO/CFO plates and BFO matrix as well as with substrates was shown in Figure 3. The incident beam was along $[0\text{-}11]_{NFO/CFO}/[010]_{BFO}$ direction. Well-defined vertical interfaces between the two constituent phases lay on {100} planes in both systems (Figs. 3(a) and (b)). Both spinel NFO and CFO plates formed {111} facets at the film surface whereas perovskite BFO matrix exhibits (001) flat surface since different crystal structures have different lowest surface energy[36,37]. Moreover, the lattice mismatch between the matrix BFO and vertical nanostructures CFO/NFO was almost relaxed at their interfaces in the present study (see Fig. S3), which are consistent with our previous studies[12,21]. Intrinsic microstructural features should be investigated further to reveal such an unusual phenomenon.

Especially, a thin BFO buffer layer between the composite thin film and the substrate was revealed in both cases. The thicknesses of BFO thin layers were about 7 nm on SRO/STO and 4 nm on DSO respectively, as shown in Fig.3(c) and (d). The results of Energy-dispersive x-ray spectroscopy (EDS) agreed well with the HRTEM observations. Taking BFO-CFO on DSO substrate as an example, the composition distribution mapping is given in Fig. 3e. An underlying thin layer containing Bi, Fe and O between CFO and DSO substrate was clearly observed. Thus the spinel phases of CFO/NFO did not grow on the substrate surface directly but were embedded in BFO matrix wholly as included plates. The interfaces between the clamped BFO thin layers and substrates marked by blue boxes in the figures were Fourier-filtered along [100] direction, as shown in the bottom of Figs. 3(c) and (d), respectively. The hetero-interfaces were almost coherent, revealing a high strain state present in the BFO buffer layer.

Quantitative analysis on the local strain state at the vicinity of

BFO-substrate heterointerfaces is shown in Fig. 4 and the standard deviations are also given. Although the experimental errors existed, the relative variations of the lattices can reveal the complex strain state in the film systems. There are little differences for the in-plane lattice parameters between the strained-BFO layer and the SRO/STO (Fig. 4a) as well as DSO substrate (Fig. 4b). The thin buffer layer of BFO was subjected to in-plane compressive stress when grown on SRO/STO substrate while tensile stress on the DSO substrate. The relative misfit can be measured to be -0.24%, 0.22% respectively, where the negative sign (-) represents compressive stress. On the other hand, the out-of plane lattice parameters of BFO at the vicinity of interfaces increased when grown on the SRO/STO substrate and decreased when deposited on DSO substrate, consisting with the analysis of in-plane strain state expected from the lattice mismatch. Such a complex strain state owing to the highly clamped underlying BFO thin layers could be responsible for the unusual combination arrangement of CFO/NFO nanostructures. One important fact has to be emphasized that the clamped layer was rarely reported in the typical perovskite-spinel nanocomposite films epitaxially grown on (001) STO substrates in previous studies, such as BFO-CFO, BTO-CFO, BFO-NFO and PTO-CFO with cube-on-cube relationships[19-23, 36]. Therefore, we focused on the strained BFO buffer layer in the subsequent discussion, which is a significant aspect that shouldn't be neglected when considering the orientation control on the spinel nanostructures.

In the vertical nanostructure systems, many factors may affect the pattern configurations during heteroepitaxial growth, such as the thermodynamic and kinetic ones (e.g. elastic energy, the anisotropy of chemical bonds in the crystal structures, interface energy, surface energy and growth parameters, etc.), among which the epitaxial strain originating from the mismatch between films and substrates as well as the crystal structure of substrates play a key role on determining the growth behavior of the nanostructure. We know that rhombohedral distorted perovskite BFO is extremely sensitive to stress, which can even reveal the ability of morphotropic phase transition due to the epitaxial strain.[27-29] The combination of strain-sensitive BFO and the substrates with different anisotropy associated with the crystal structure would impose a complex strain state on the included nanostructures which may affect their nucleation and the dynamic growth behavior. A possible growth mechanism is proposed based on the experimental observations and the strain state analysis for the present study. Figure 5 schematically shows the formation of [011] orientated nanostructures in the two film systems by three stages of growth.

With the fluctuation of deposition conditions of films at the initial growth stage [Fig. 5a], for example a bit higher deposition rate or temperature, it's reasonable to presume that BFO crystalline prefer to wet the surface of substrate and spread quickly since it has the same perovskite structure and lower nucleation barrier on perovskite substrate. Meanwhile, the spinel phase won't start to nucleate immediately due to two main reasons. One is the large structure difference between the cubic spinel and the orthorhombically distorted perovskite substrate. Another point lies in that polyhedral spinel crystal with low surface energy reconstruction needs some times to collect a certain amount of spinel species[38]. Therefore, thin BFO buffered layers formed coherently on the surface of the substrates at the early stage of deposition [Fig. 5(b)], which can be observed in Fig. 3(c) and 3(d). A key question regarding strain thus came out: can the misfit strain in the BFO buffered layer be released by the formation of dislocations or not? For hetero-epitaxial thin films, the calculated critical thickness for forming misfit dislocations can be described by the following formula based on Matthews and Blakeslee theory:[39, 40]

$$h_c = \frac{b}{8\pi(1+\nu)f}\left[\ln\left(\frac{h_c}{b}\right)+1\right] \quad (1)$$

where ν is Poisson's ratio, f is the relative misfit, and b is Burgers vector of misfit dislocations. Setting ν=0.25, a typical value for oxides[39]; Burgers vector b can be considered to be $a_{[010]}$ of substrate (~0.394nm); h_c is estimated to be about 9.4 nm for the ~0.55% nominal mismatch of BFO and DSO or SRO. Thus the thickness of BFO buffer layer in the present study, smaller than 7 nm in both systems, did not exceed the critical thickness as the theoretical prediction. Therefore, BFO thin layer is clamped by the substrate almost coherently, suggesting that it is under a state of biaxial tensile/compressive constraints imposed by the heteroepitaxy. Therefore, octahedral tilting and rotation in the orthorhombic distorted perovskite substrates can easily impact on the BFO thin layer.

As the deposition process goes on at a high temperature of 700 ℃, spinel nucleus of NFO/CFO might aggregate and start to grow on the surface of highly strained BFO buffer layer, as shown in Fig. 5(b). The crystalline of NFO/CFO elongated along <0-11> in-plane directions due to the preferential motion of the spinel ledges with lower activation energy, which is called the ledge growth mechanism[35]. On the other hand, orthorhombically distorted DSO substrate provides an anisotropic characteristic and octahedron distortion. It can apply a similar anisotropic stress on the above BFO thin layer which results in the in-plane unequivalent stress in BFO even if it is equivalent in bulk structure. Correspondingly, the above CFO elongated along one of its <110> directions and formed anisotropic nano-plate structure with the [011] orientation shown in Fig. 5c. 2-D nanostructure, however, was observed when similar BFO-NFO composite films grew on the SRO/STO substrate. The in-plane anisotropy of SRO is much smaller than that of DSO compared from their lattice parameters. Therefore, the clamped BFO and hence the above NFO nanostructure grew along two <110> directions which create 2-D structural variants perpendicular to each other [Fig. 5d].

The anisotropic elongations of vertical nanostructures and regulations on the crystallographic orientation may provide plentiful choices to design strong correlated complex oxides. The tunable nanostructures may enable the control of material functionalities such as the magnetic anisotropy of CFO with the fixed elongation direction, which would demonstrate a great potential application in next generation electromagnetic devices.

4. Conclusions

In summary, we have demonstrated the nano-plate configurations with defined heterointerface structures and misorientation relationships in the $BiFeO_3$-$CoFe_2O_4$ and $BiFeO_3$-$NiFe_2O_4$

perovskite-spinel model systems when grown on $[001]_c$ oriented SRO/STO and DSO substrates respectively. The spinel nano-plates elongated along $<110>_{NFO/CFO}$ directions with anisotropic distributions were fully embedded in the BFO matrix and their crystal orientations were tuned to [011] along the growth direction, with BFO keeping the cube-on-cube orientation relationship with the perovskite substrates. A highly strained thin BFO buffer layer was introduced between spinel plates and the substrates to determine the initial growth of the spinel nano-plates. The manipulations of the vertical nanostructures in both film systems can be attributed to the complicated strain state in the film systems and the preferential motions of spinel structure along the <110> ledges.

Acknowledgement

This work is supported by the program of National Basic Research Development Plan with Grant 2011GB108002, 2011CB606406, and the National Natural Science Foundation of China with Grant Nos. 51371031, 50971015, 51071092. The work in National Chiao Tung University is supported by the National Science Council, R.O.C. (NSC-101–2119-M-009–003-MY2), Ministry of Education, R.O.C. (MOE-ATU 101W961), and Center for interdisciplinary science of National Chiao Tung University. The authors gratefully acknowledge Professor R. Ramesh and Dr. S.P. Crane of University of California, Berkeley for their provision of a part of the samples.

Supplementary Information

The schematic of 3-D relationships in the perovskite-spinel systems and the related HRTEM images are available.

Notes and references

[a]*School of Materials Science and Engineering, University of Science and Technology Beijing, Beijing 100083, China. E-mail: qzhan@mater.ustb.edu.cn*
[b]*Beijing National Center for Electron Microscopy, Department of Materials Science and Engineering, Tsinghua University, Beijing 100084, China E-mail: Ryu@tsinghua.edu.cn*
[c]*Department of Materials Science and Engineering, National Chiao Tung University, Hsinchu 30010, Taiwan. E-mail: yhc@nctu.edu.tw*
[d]*Institute of Physics, Academia Sinica, Taipei 105, Taiwan*

1. S. Wu, S. A. Cybart, P. Yu, M. Rossell, J. Zhang, R. Ramesh and R. Dynes, *Nat. Mater.*, 2010, **9**, 756-761.
2. J. L. MacManus-Driscoll, *Adv. Funct. Mater.*, 2010, **20**, 2035-2045.
3. L. W. Martin and R. Ramesh, *Acta Mater.*, 2012, **60**, 2449-2470.
4. H. Zheng, J. Wang, S. E. Lofland, Z. Ma, L. Mohaddes-Ardabili, T. Zhao, L. Salamanca-Riba, S. R. Shinde, S. B. Ogale, F. Bai, D. Viehland, Y. Jia, D. G. Schlom, M. Wuttig, A. Roytburd; and R. Ramesh, *Science*, 2004, **303**, 661-663.
5. Y.-J. Chen, Y.-H. Hsieh, S.-C. Liao, Z. Hu, M.-J. Huang, W.-C. Kuo, Y.-Y. Chin, T.-M. Uen, J.-Y. Juang, C.-H. Lai, H.-J. Lin, C.-T. Chen and Y.-H. Chu, *Nanoscale*, 2013, **5**, 4449-4453.
6. J. Li, I. Levin, J. Slutsker, V. Provenzano, P. K. Schenck, R. Ramesh, J. Ouyang and A. L. Roytburd, *Appl. Phys. Lett.*, 2005, **87**, 072909.
7. S. A. Harrington, J. Zhai, S. Denev, V. Gopalan, H. Wang, Z. Bi, S. A. T. Redfern, S. H. Baek, C. W. Bark and C. B. Eom, *Nat. Nanotechnol.*, 2011, **6**, 491-495.
8. A. Chen, Z. Bi, H. Hazariwala, X. Zhang, Q. Su, L. Chen, Q. Jia, J. L. MacManus-Driscoll and H. Wang, *Nanotechnology*, 2011, **22**, 315712.
9. W. Chang, J. S. Horwitz, A. C. Carter, J. M. Pond, S. W. Kirchoefer, C. M. Gilmore and D. B. Chrisey, *Appl. Phys. Lett.*, 1999, **74**, 1033.
10. Z. Bi, E. Weal, H. Luo, A. Chen, J. L. MacManus-Driscoll, Q. Jia and H. Wang, *J. Appl. Phys.*, 2011, **109**, 054302.
11. N. Dix, R. Muralidharan, J. M. Rebled, S. Estradé, F. Peiró, M. Varela, J. Fontcuberta and F. Sánchez, *ACS Nano*, 2010, **4**, 4955.
12. Y. M. Zhu, D. Ke, R. Yu, Y. H. Hsieh, H. J. Liu, P. P. Liu, Y. H. Chu and Q. Zhan, *Appl. Phys. Lett.*, 2013, **102**, 111903.
13. B. Mercey, M. Hervieu, W. Prellier, J. Wolfman, C. Simon and B. Raveau, *Appl. Phys. Lett.*, 2001, **78**, 3857.
14. D. G. Schlom, L.-Q. Chen, C.-B. Eom, K. M. Rabe, S. K. Streiffer and J.-M. Triscone, *Annual Review of Materials Research*, 2007, **37**, 589-626.
15. A. Mukherjee, W. S. Cole, P. Woodward, M. Randeria and N. Trivedi, *Phys. Rev. Lett.*, 2013, **110**, 157201.
16. J. Gazquez, S. Bose, M. Sharma, M. A. Torija, S. J. Pennycook, C. Leighton and M. Varela, *APL Materials*, 2013, **1**, 012105.
17. A. Artemev, J. Slutsker and A. L. Roytburd, *Acta Mater.*, 2005, **53**, 3425-3432.
18. J. Slutsker, I. Levin, J. Li, A. Artemev and A. Roytburd, *Physical Review B*, 2006, **73**, 184127.
19. I. Levin, J. Li, J. Slutsker and A. L. Roytburd, *Adv. Mater.*, 2006, **18**, 2044-2047.
20. Z. Tan, J. Slutsker and A. L. Roytburd, *J. Appl. Phys.*, 2009, **105**, 061615.
21. Q. Zhan, R. Yu, S. P. Crane, H. Zheng, C. Kisielowski and R. Ramesh, *Appl. Phys. Lett.*, 2006, **89**, 172902.
22. I. Fina, N. Dix, L. Fàbrega, F. Sánchez and J. Fontcuberta, *J. Appl. Phys.*, 2010, **108**, 034108.
23. H. Zheng, F. Straub, Q. Zhan, P. L. Yang, W. K. Hsieh, F. Zavaliche, Y. H. Chu, U. Dahmen and R. Ramesh, *Adv. Mater.*, 2006, **18**, 2747-2752.
24. H. Zheng, J. Wang, L. Mohaddes-Ardabili, M. Wuttig, L. Salamanca-Riba, D. G. Schlom and R. Ramesh, *Appl. Phys. Lett.*, 2004, **85**, 2035.
25. N. M. Aimon, D. Hun Kim, H. Kyoon Choi and C. A. Ross, *Appl. Phys. Lett.*, 2012, **100**, 092901.
26. S. C. Liao, P. Y. Tsai, C. W. Liang, H. J. Liu, J. C. Yang, S. J. Lin, C. H. Lai and Y. H. Chu, *ACS Nano*, 2011, **5**, 4118-4122.
27. R. J. Zeches, M. D. Rossell, J. X. Zhang, A. J. Hatt, Q. He, C. H. Yang, A. Kumar, C. H. Wang, A. Melville, C. Adamo, G. Sheng, Y. H. Chu, J. F. Ihlefeld, R. Erni, C. Ederer, V. Gopalan, L. Q. Chen, D. G. Schlom, N. A. Spaldin, L. W. Martin and R. Ramesh, *Science*, 2009, **326**, 977-980.
28. I. C. Infante, S. Lisenkov, B. Dupé, M. Bibes, S. Fusil, E. Jacquet, G. Geneste, S. Petit, A. Courtial, J. Juraszek, L. Bellaiche, A. Barthélémy and B. Dkhil, *Phys. Rev. Lett.*, 2010, **105**, 057601.
29. J. Yang, Q. He, S. Suresha, C. Kuo, C. Peng, R. Haislmaier, M. Motyka, G. Sheng, C. Adamo and H. Lin, *Phys. Rev. Lett.*, 2012, **109**, 247606.
30. J. Moreau, C. Michel, R. Gerson and W. James, *J. Phys. Chem. Solids*, 1971, **32**, 1315-1320.
31. K. Subramanyam, *J. Phys. C: Solid State Phys.*, 1971, **4**, 2266.
32. A. Goldman, *Modern Ferrite Technology*, Springer, 2006, p55.
33. B. J. Kennedy and B. A. Hunter, *Physical Review B*, 1998, **58**, 653-658.
34. Price and McCarthy, Penn State University, University Park, Pennsylvania, ICDD Grand-in-Aid 1974 (x-ray data base file ID27–0204).
35. S. V. Yanina and C. Barry Carter, *Surf. Sci.*, 2002, **513**, L402-L412.
36. H. Zheng, Q. Zhan, F. Zavaliche, M. Sherburne, F. Straub, M. P. Cruz, L. Q. Chen, U. Dahmen and R. Ramesh, *Nano Lett.*, 2006, **6**, 1401-1407.
37. G. Wulff; and Z. Kristallogr;, *Mineral*, 1901, **34**, 449-530.
38. Y.-H. Hsieh, H.-H. Kuo, S.-C. Liao, H.-J. Liu, Y.-J. Chen, H.-J. Lin, C.-T. Chen, C.-H. Lai, Q. Zhan, Y.-L. Chueh and Y.-H. Chu, *Nanoscale*, 2013, **5**, 6219.
39. X. Qi, M. Wei, Y. Lin, Q. Jia, D. Zhi, J. Dho, M. G. Blamire and J. L. MacManus-Driscoll, *Appl. Phys. Lett.*, 2005, **86**, 071913.
40. J. Matthews and A. Blakeslee, *J. Cryst. Growth*, 1974, **27**, 118-125.

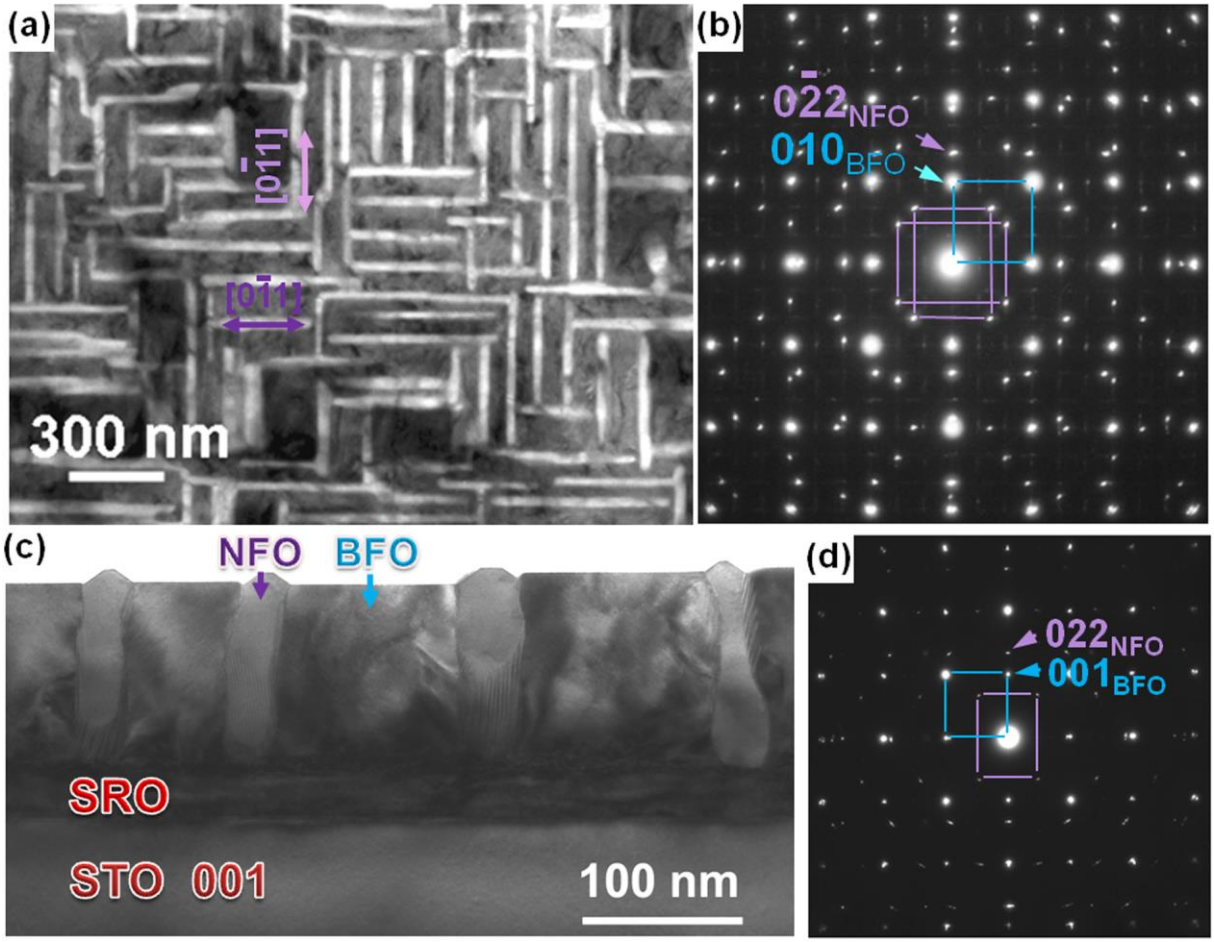

Fig. 1 (a) and (b) Plan-view TEM of BFO-NFO nanostructure and corresponding diffraction patterns. (c) Cross-sectional TEM image showing NFO inclusions embedded in BFO matrix of films grown on (001) STO substrate with a ~30 nm thick SRO transition layer. (d) Selected area diffraction pattern from (c) with [010] BFO direction.

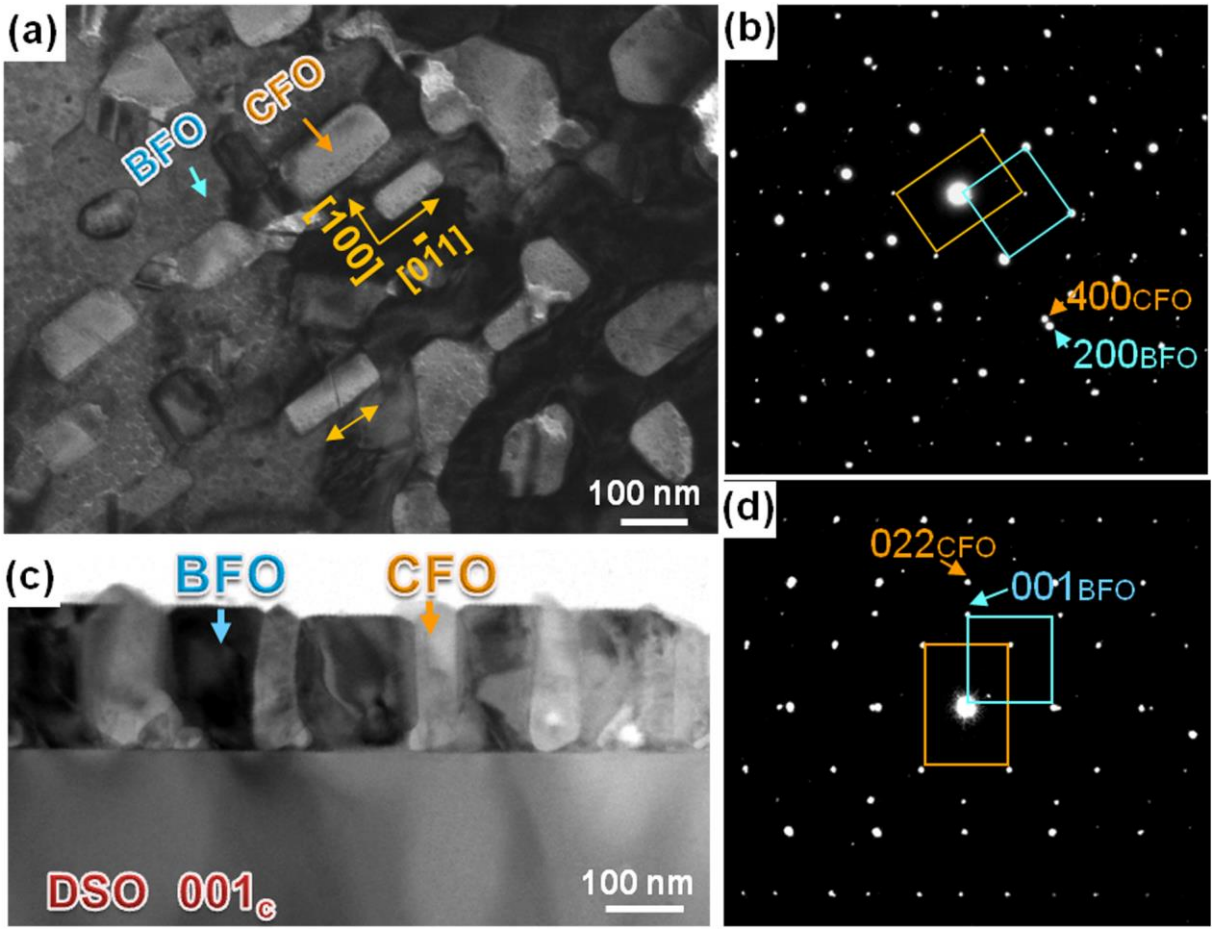

Fig. 2 The typical TEM morphologies of the $BiFeO_3$-$CoFe_2O_4$ thin film grown on $DyScO_3$ substrate from (a) plan-view from [001]BFO/[011]CFO direction and (c) cross-sectional of CFO [0-11] directions. (b) and (d) show the corresponding electron diffraction patterns of the plan-view (a) and cross-section (c).

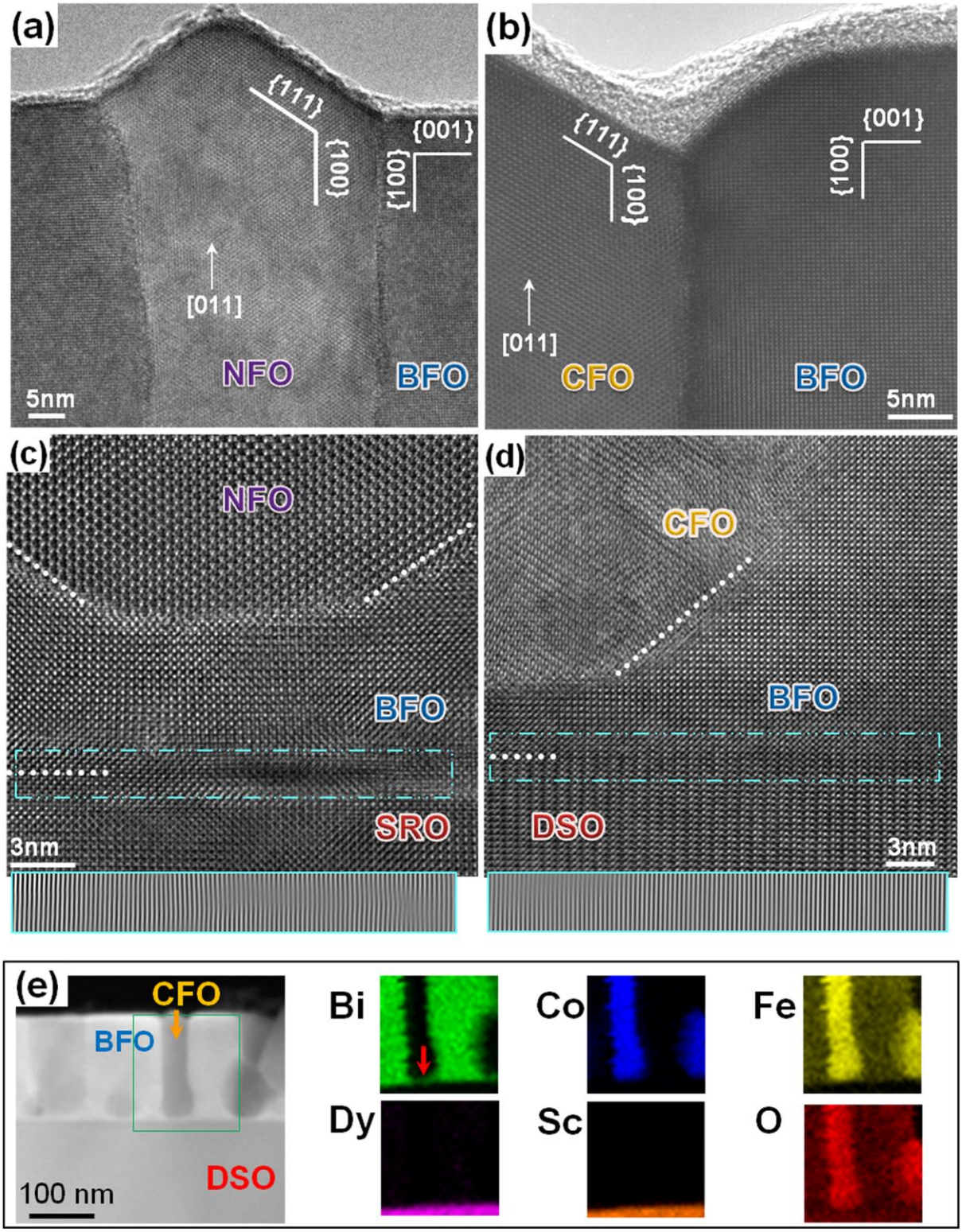

Fig. 3 High resolution cross-sectional images of the BFO-CFO/NFO films on different substrates. (a) and (b) BFO-CFO interface at the film surface, BFO-NFO interface at the film surface, respectively. (c) NFO-BFO-SRO interfaces closed to the substrate showing a 7 nm thick-BFO layer coherent with SRO surface but semi-coherent with NFO phase. (d) CFO-BFO-DSO interface, showing a BFO thin layer of 4 nm. Bottom insets in (c) and (d) are the one-dimensional FFT filtered images of dashed boxes. (e) EDS data of BFO-CFO films grown on DSO substrate. It shows the cross-sectional HAADF image and the corresponding elemental maps of Bi, Co, Fe, Dy, Sc and O obtained from the area marked by a green square.

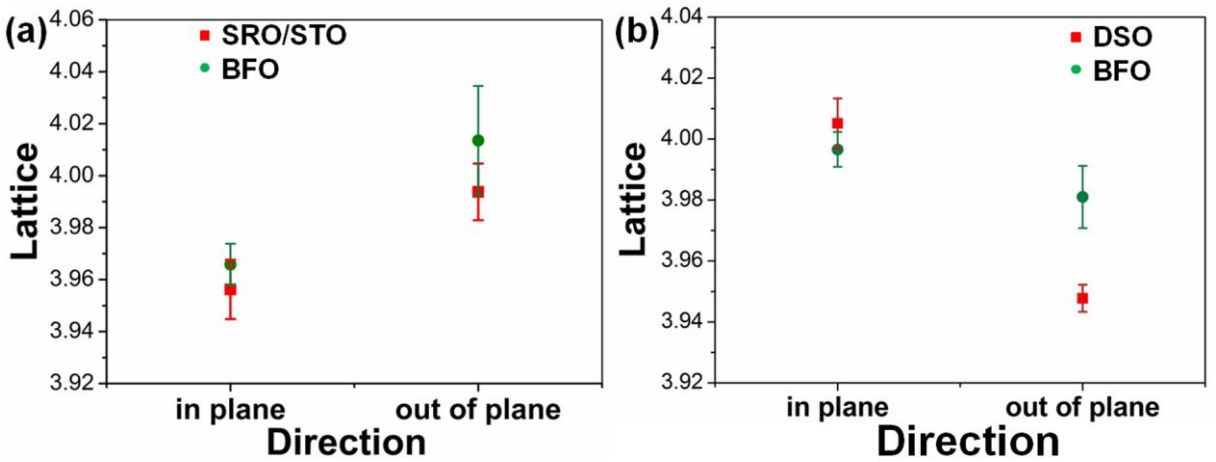

Fig. 4 Lattice parameters measured at the bottom interfaces of (a) BFO-SRO/STO and (b) BFO-DSO in both systems from the cross-sectional HRTEM images.

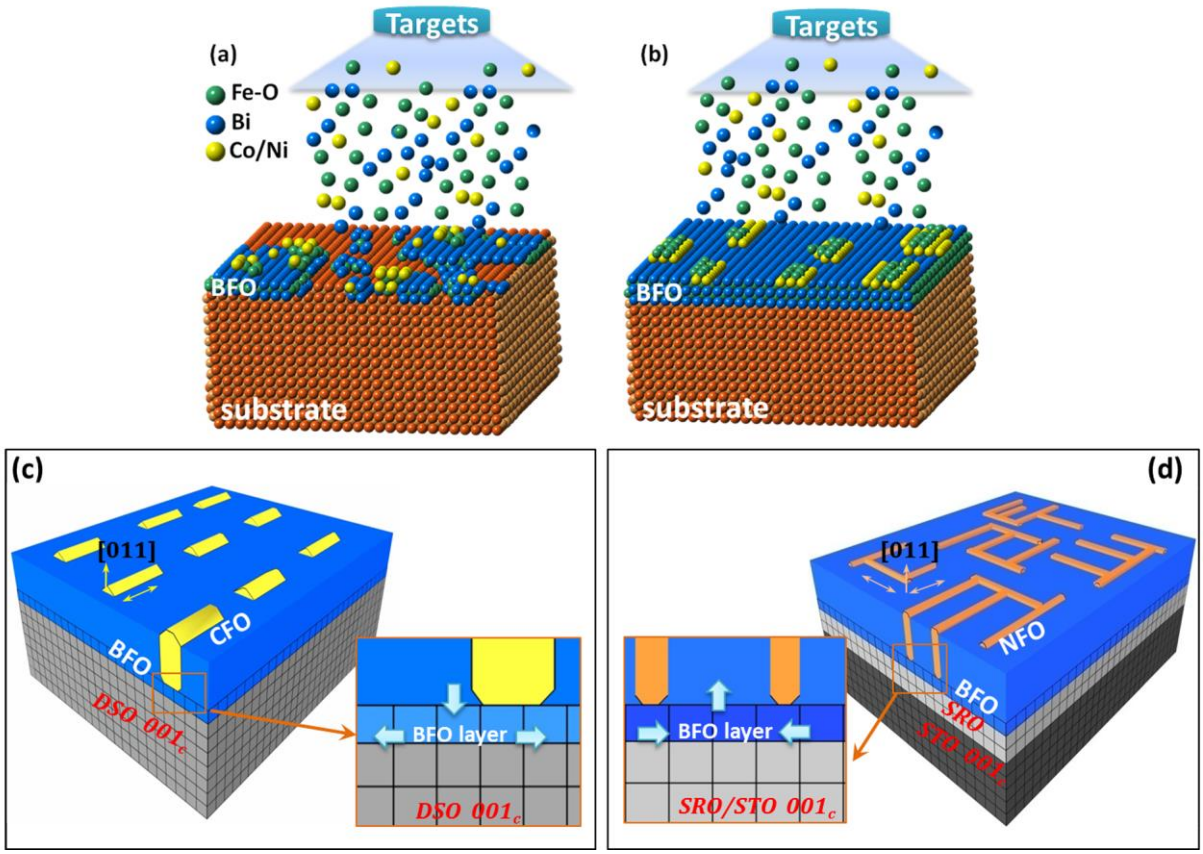

Fig. 5 Schematic model of the growth procedure with three deposition stages. (a) Thin BFO phase wetting the substrates. (b) Spinel phases nucleation on BFO buffer layers. (c) CFO nano-plate islands formed in BFO matrix. (d) NFO nano-plates formed in BFO matrix. The enlarged insects of (c) and (d) show coherent BFO buffer layer and the corresponding strain state analysis from Fig.4.

Tables of Contents Entry

The orientation tuning of heterostructures combined the nano-plate configuration were demonstrated by the complex in-plane strain and ledge growth mechanism.

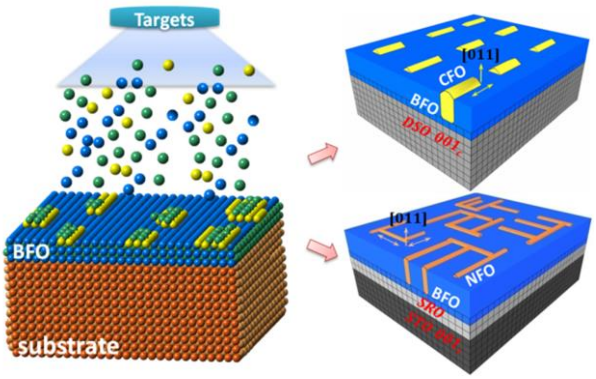

Supplementary Information:

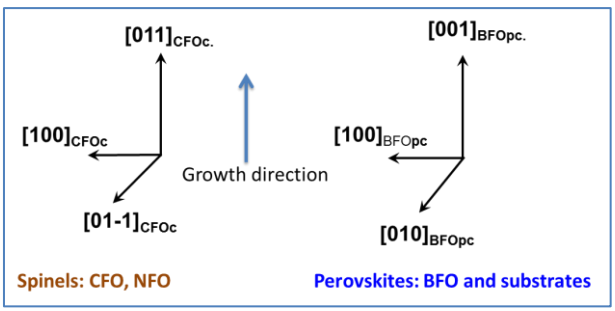

Fig.S1 A schematic of 3-D relationships in the perovskite-spinel systems.

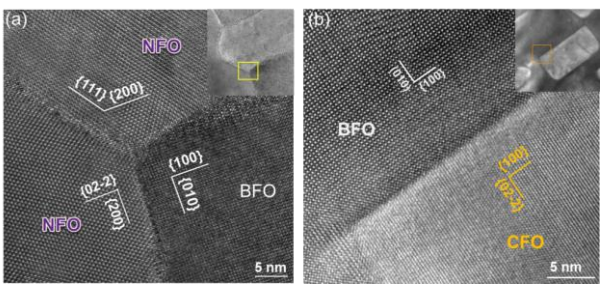

Fig.S2 Plan-view HRTEM from BFO[001] and [011]NFO/CFO directions.

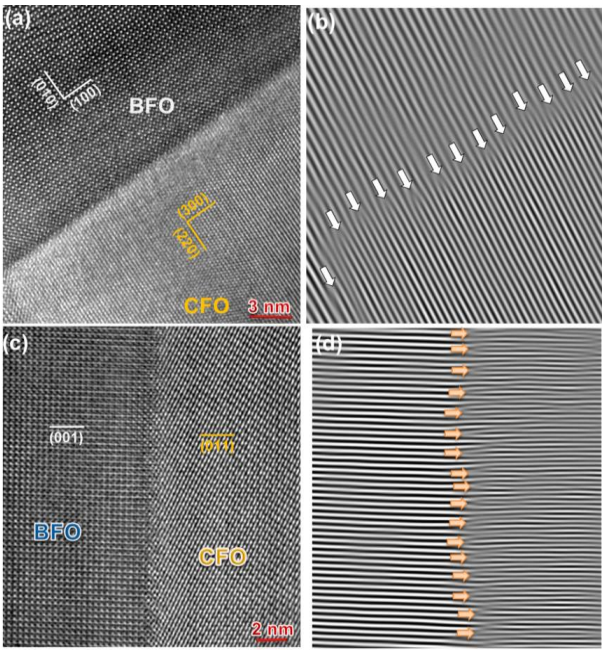

Fig. S3 the BFO-CFO interfaces with one-dimensional FFT filtered images, (a) and (b) plane-view, (c) and (d) cross-section